Journal of Materials Chemistry A

Accepted Manuscript

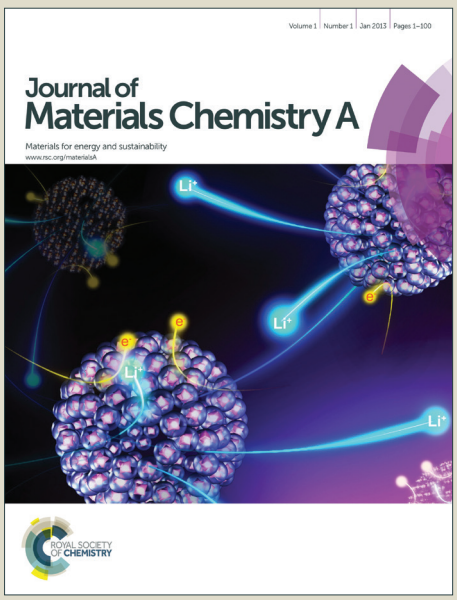

ROYAL SOCIETY OF CHEMISTRY

www.rsc.org/materialsA

Journal of Materials Chemistry A

Cite this: DOI: 10.1039/c0xx00000x

Paper

www.rsc.org/xxxxxx

Sn-stabilized Li-rich layered $Li(Li_{0.17}Ni_{0.25}Mn_{0.58})O_2$ oxide as cathode for advanced lithium-ion batteries

Qi-Qi Qiao,[a] Lei Qin,[a] Guo-Ran Li,[a] Yong-Long Wang[a] and Xue-Ping Gao*[a,b]

Received (in XXX, XXX) Xth XXXXXXXXX 20XX, Accepted Xth XXXXXXXXX 20XX

DOI: 10.1039/b000000x

Li-rich layered oxides have been intensively investigated as cathode for high energy lithium-ion batteries. However, oxygen loss from the lattice in the initial charge and the gradual structural transformation during cycling can lead to a capacity degradation and potential decay for the cathode materials. In this work, Sn^{4+} is used to partially substitute Mn^{4+} to prepare a series of $Li(Li_{0.17}Ni_{0.25}Mn_{0.58-x}Sn_x)O_2$ (x = 0, 0.01, 0.03, and 0.05) samples through a spray-drying method. Structure characterization reveals that the Sn^{4+} substituted samples with a suitable amount show a low cation mixing, indicating an enhanced ordered layer structure. Moreover, the metal-oxygen (M-O) covalency is gradually decreased with increasing Sn^{4+} amount. It is shown from the initial charge-discharge curves that Sn^{4+} substituted samples present a shorter charging potential plateau at 4.5 V (vs Li/Li^+), implying that oxidation of the O^{2-} ion to O_2 is suppressed by Sn^{4+} substitution and lead to the minor structural change. Among the Sn^{4+} substituted samples, the $Li(Li_{0.17}Ni_{0.25}Mn_{0.55}Sn_{0.03})O_2$ sample exhibits a higher capacity retation of 86% after 400 cycles at 0.1 C rate and 92 % after 200 cycles at 1 C rate, showing an excellent cycle stability and high-rate capability as compared with the as-prepared sample. The electrochemical performance improvement can be attributed to the influence of Sn such as enlarging Li ion diffusion channel due to large ionic radius of Sn^{4+} substitution with respect to Mn^{4+}, higher bonding energy of Sn-O than Mn-O, and weakening M-O covalency. All the influence is favorable for stabilization of the host lattice in Li-rich layered oxides.

Introduction

Lithium-ion batteries have been widely applied to portable electronic products, electric vehicles (EVs) and hybrid electric vehicles (HEVs). The demand of high energy density, long cycle life, low cost and safe battery has become indispensable.[1-3] Cathode materials as the key constituent part of lithium-ion batteries play a crucial role in determining the whole battery performance. Therefore, it is highly significant to develop cathode materials with large specific capacity to fulfill the requirements for advanced lithium-ion batteries. Recently, Li-rich layered oxides have attracted particular attention,[4-8] due to their large specific capacity of over 250 mAh g^{-1} as compared with cathode materials in the current commercial lithium-ion batteries, such as layered $LiCoO_2$, spinel $LiMn_2O_4$, and olivine $LiFePO_4$.

Li-rich layered oxides, denoted as $Li(Li_{1/3-2x/3}Ni_xMn_{2/3-x/3})O_2$ or $xLi_2MnO_3{\cdot}(1\text{-}x)LiMO_2$ (M represents transition metal), are intercalated nanocomposites consisting of two different local structures: $LiMO_2$ phase (space group: $R\bar{3}m$) and the monoclinic Li_2MnO_3 phase (space group: C2/m).[9] The initial electrochemical reaction mechanism of Li-rich layered oxides is different from that of the current lithium intercalation cathodes. When the initial charge potential is low than 4.5 V (vs Li/Li^+), the electrochemically inert Li_2MnO_3 component is required to stabilize the structure of layered oxides. The high capacity originates from the activation of Li_2MnO_3 and the deintercalation of Li_2O from the layered lattice at above 4.5 V (vs Li/Li^+). It is demonstrated that oxygen is released from the layered lattice at the end of the initial charging, accompanied with the generation of oxygen vacancies, then the transition metal ions are moved into the leaving vacancies due to the lithium-ion deintercalation from transition metal layers.[10] The oxygen loss in Li-rich layered oxides can bring a series of problems such as large initial irreversible capacity loss, unstable structure on account of ion rearrangements, and oxidation of electrolyte. In order to solve these problems, many efforts and attempts have been implemented such as surface modification with carbon and conductive polymer,[11,12] metal oxides,[13-15] fluorides,[6,16] and phosphates,[17] ion substitution or doping, and morphology control of particles or grains.[18-20] In particular, partial substitution with cation (Na^+, Mg^{2+}, Y^{3+}, Al^{3+}, Cr^{3+}, Ti^{4+}, and Ru^{4+})[21-25] or doping with polyanion (PO_4^{3-} and BO_4^{5-})[26,27] is proved to be effective for improving the electrochemical performance of Li-rich layered oxides. Generally, these substitution or doping ions should have large ionic radius and high electronegativity, in order to expand the lithium ion diffusion channel and decrease the M-O covalency in Li-rich layered oxides. Correspondingly, the oxygen

evolution is suppressed by ion substitution with a minor structural change, which is favorable for the stabilization of the host lattice in Li-rich layered oxides.

Sn^{4+} has a ionic radius of 0.69 Å, larger than that of Mn^{4+} (0.53 Å). Meanwhile, the bonding energy of Sn-O (548 kJ mol^{-1}) is higher than that of Mn-O (402 kJ mol^{-1}), which is helpful to enhance the structural stability. More importantly, the Sn^{4+} cation has higher electronegativity with respect to Mn^{4+} cation, leading to the stronger ionicity of Sn-O bond as compared to that of Mn-O bond. In this work, Sn^{4+} is introduced to partially substitute Mn^{4+} in the Li-rich layered $Li(Li_{0.17}Ni_{0.25}Mn_{0.58})O_2$ oxide. The resulting samples are characterized and the electrochemical performances are measured in detail. It is expected that the Sn^{4+} substitution can improve cycle stability of the Li-rich layered oxides.

Experimental

Preparation and characterization

$Li(Li_{0.17}Ni_{0.25}Mn_{0.58-x}Sn_x)O_2$ (x = 0, 0.01, 0.03, and 0.05) powders were prepared by combining spray-drying and solid-state reaction. Stoichiometric amount of manganese and nickel acetate tetrahydrates, tin chloride dihydrate and an excessive amount of lithium hydroxide monohydrate 8% (mole ratio) were dissolved in distilled water to obtain a mixed solution. Then, the mixed solution was dropped slowly into citric acid solution with continuously stirring. Here, citric acid was used as a chelating agent to complex with transition metal ions (Ni, Mn, and Sn citrates) in order to insure the formation of the homogeneous aqueous solution. The solution pH was adjusted at 9 by ammonia solution. The resulting solution was pumped into a spray drying instrument (L217, LaiHeng) to produce homogenous precursor. The precursor was initially decomposed at 480 °C for 5 h in air. After being ground, the resulting powders were put into a corundum crucible and calcined again at 850 °C for 10 h in air, and quenched in water, cooled to obtain the $Li(Li_{0.17}Ni_{0.25}Mn_{0.58-x}Sn_x)O_2$ samples (x = 0, 0.01, 0.03, and 0.05). The samples were marked as LNMO, LNMO-$Sn_{0.01}$, LNMO-$Sn_{0.03}$, and LNMO-$Sn_{0.05}$, respectively. The structure, morphology and surface state of the samples were detected using X-ray diffraction (XRD, Rigaku D/MAX-2500v/pc), scanning electron microscopy (SEM, SUPRA 55VP), transmission electron microscopy (TEM, FEI Tecnai F20), Fourier transform infrared spectra (FTIR, Bruker Tensor 27), and X-ray photoelectron spectroscopy (XPS, PHI5000 VersaProbe). Thermal stability of the electrode at the charged state after the initial charge to 4.8 V (vs Li/Li^+) was analyzed by differential scanning calorimetry (DSC, Mettler Toledo) using a sealed high-pressure DSC pan.

Electrochemical measurement

The obtained samples, acetylene black (as conductive agent), and polytetrafluoroethylene (PTFE, as binder) were mixed at a weight ratio of 75:15:10, and compressed to prepare the working electrode. The electrode loading mass for the active material in each cell is 4.97 mg cm^{-2}. The current density of 30 mA g^{-1} (0.1 C) corresponds to 0.15 mA cm^{-2}. A metallic lithium foil was used as the counter and reference electrodes. The half cell was composed of a cathode and a lithium metal anode separated by a Celgard 2400 porous polypropylene film separator. The electrolyte was $LiPF_6$ (1M) in a mixture of ethylene carbonate (EC) and dimethyl carbonate (DMC) with a volume ratio of 3:7. The galvanostatic charge and discharge tests were performed between 2.0 and 4.8 V (vs. Li/Li^+) with LAND CT-2001A instrument (Wuhan, China) at room temperature. The cyclic voltammetry (CV) measurement was conducted with a CHI 600A electrochemical workstation at a scan rate of 0.1 mV s^{-1}. Electrochemical impedance spectra (EIS) were measured using a Zahner IM6ex electrochemical workstation in the frequency range of 100 kHz to 10 mHz.

Results and discussion

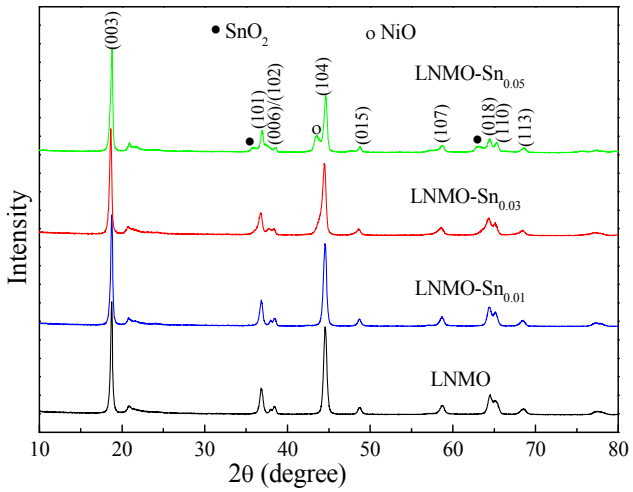

Fig. 1 XRD patterns of the LNMO, LNMO-$Sn_{0.01}$, LNMO-$Sn_{0.03}$, and LNMO-$Sn_{0.05}$ samples.

Fig. 1 shows XRD patterns of the LNMO, LNMO-$Sn_{0.01}$, LNMO-$Sn_{0.03}$, and LNMO-$Sn_{0.05}$ samples. All the main peaks in the patterns are indexed as the O3 type layered structure with R $\bar{3}$ m space group. The weak peaks around 2θ = 20–25° correspond to the Li_2MnO_3 and the ordering of Li, Ni, and Mn atoms in the transition metal layers.[28-30] The Rietveld refinement of XRD data of LNMO and LNMO-$Sn_{0.01}$ samples is performed with General Structure Analysis System (GSAS) software as shown in **Fig. S1**. XRD patterns can be refined with two different local structures of R $\bar{3}$ m and monoclinic phases. In order to verify the substitution of Sn^{4+} for Mn^{4+}, the refinement is conducted based on the atomic occupancies of Sn atoms on Mn positions in the layered structure. When the excessive Sn^{4+} is added into the sample, the SnO_2 could be formed and precipitated due to the larger ionic radius of Sn^{4+}. Therefore, for the LNMO-$Sn_{0.05}$ sample, the low diffraction peaks of impurities are observed at 2θ = 36°, 43° and 63°, which are assigned to the NiO and SnO_2, suggesting the crystallographic structure of the LNMO oxide is partially destroyed after the more substitution of Sn^{4+} for Mn^{4+}. Generally, the intensity ratio of $I_{(003)}/I_{(104)}$ in XRD patterns can be used to characterize the degree of cation mixing in Li-rich layered oxides.[31] Here, the intensity ratio of $I_{(003)}/I_{(104)}$ increases from 1.278 for the LNMO sample to 1.344, 1.475 and 1.811 for the LNMO-$Sn_{0.01}$, LNMO-$Sn_{0.03}$ and LNMO-$Sn_{0.05}$ samples, respectively, indicating the lower cation mixing (especially for Li^+/Ni^{2+} mixing) and more ordered layer structure after Sn^{4+} substitution for Mn^{4+}. The lattice parameters of all the samples are refined according to hexagonal structure based on R $\bar{3}$ m space

group and shown in **Table 1**. The *a* usually stand for the transition metal-oxygen slab and *c* represents the interspacing of transition metal layers.[22,23] The LNMO-$Sn_{0.03}$ sample shows the largest *c*-lattice parameter and *c*/*a* ratio, indicating the largest lithium ion diffusion channels and more perfect layer structure in Li-rich layered oxides. However, the *c* and *c*/*a* values of the LNMO-$Sn_{0.01}$ sample are slightly decreased as compared with the LNMO, probably due to higher bonding energy of Sn-O and the shorter length of Sn-O than Mn-O.[32]

Table 1 The crystallographic parameters of all the samples

Sample	*a*/Å	*c*/Å	*c*/*a*	$I_{(003)}/I_{(104)}$
LNMO	2.8551	14.2293	4.9838	1.278
LNMO-$Sn_{0.01}$	2.8606	14.2252	4.9728	1.344
LNMO-$Sn_{0.03}$	2.8605	14.2742	4.9901	1.475
LNMO-$Sn_{0.05}$	2.8543	14.2368	4.9878	1.811

The surface morphology and size distribution of the as-prepared LNMO and Sn^{4+} substituted samples are examined by SEM (Fig. 2). The LNMO sample exists as loose aggregates, which are assembled from the sphere-like grains with a diameter of 100~200 nm. There is almost no change in the morphology and particle sizes after Sn^{4+} substitution for Mn^{4+}, however, the grains of LNMO-$Sn_{0.05}$ sample have some extent agglomeration, may be resulted from the impurities NiO and SnO_2. The EDS mappings of Ni, Mn, Sn and O in the LNMO-$Sn_{0.03}$ samples are provided in **Fig. S3**. The Sn is uniformly distributed in the entire particle. The detailed composition for representative particles is shown in **Table S7** and **S8** by ICP-MS test. The chemical compositions of the LNMO and LNMO-$Sn_{0.03}$ samples are $Li_{1.21}Ni_{0.24}Mn_{0.51}O_2$ and $Li_{1.16}Ni_{0.24}Mn_{0.48}Sn_{0.02}O_2$, respectively.

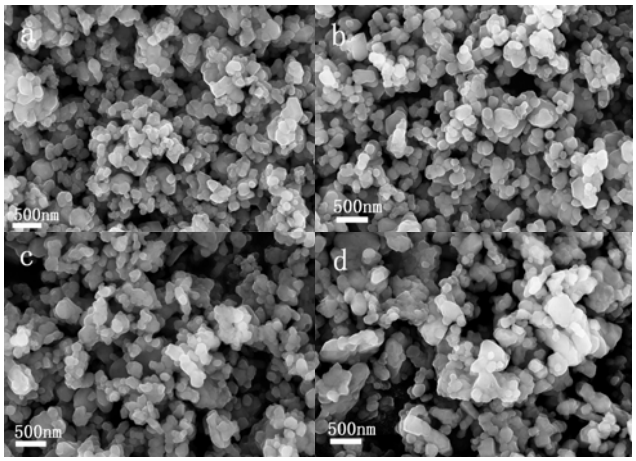

Fig. 2 SEM images of (a) LNMO, (b) LNMO-$Sn_{0.01}$, (c) LNMO-$Sn_{0.03}$, and (d) LNMO-$Sn_{0.05}$ samples.

HRTEM images of the LNMO, LNMO-$Sn_{0.01}$, LNMO-$Sn_{0.03}$, and LNMO-$Sn_{0.05}$ samples are displayed in **Fig. 3**. All the images show clear lattice fringes with *d* spacing of 0.47 nm, corresponding to the interplanar distance of the (003) plane in the XRD patterns.[21,33,34] It is deduced that all the samples have good crystallinity, while a few lattice defects coexist with crystalline lattices in the Sn^{4+} substituted samples owing to the slight altering of the local environment by Sn^{4+} substitution for Mn^{4+}. The Fast Fourier Transform (FFT) and Inverse Fast Fourier Transform (IFFT) are added in the selected area, which is almost identical to the selected area electron diffraction (SAED). For the LNMO-$Sn_{0.01}$ sample, the brightness of lattice fringes is homogeneous, only a little fringes become bent due to the slight local strain arised by the substitution of larger Sn^{4+} (in the IFFT of Fig. 3b). When the Sn^{4+} amount is further increased, Sn-rich dark areas can be observed clearly from the IFFT images of LNMO-$Sn_{0.03}$ and LNMO-$Sn_{0.05}$ samples (as noted with white arrows in image c and d) according to mass-thickness contrast, which are commonly found in the element substitution or doping of oxides.[35] It should be noted that SnO_2 impurities would appear in dark areas with more Sn substitution, in coincident with XRD analysis. The analogous result is observed in the Li-rich layered $Li(Li_{0.17}Ni_{0.20}Co_{0.05}Mn_{0.58})O_2$ oxide after doping with PO_4^{3-} polyanion.[26] The larger ionic radius and the stronger M-O bond of Sn^{4+} substituted samples lead to more stable layered structure. The substitution could restrain the O^{2-} anions migration to the surface by utilizing the higher Sn-O bond energy.

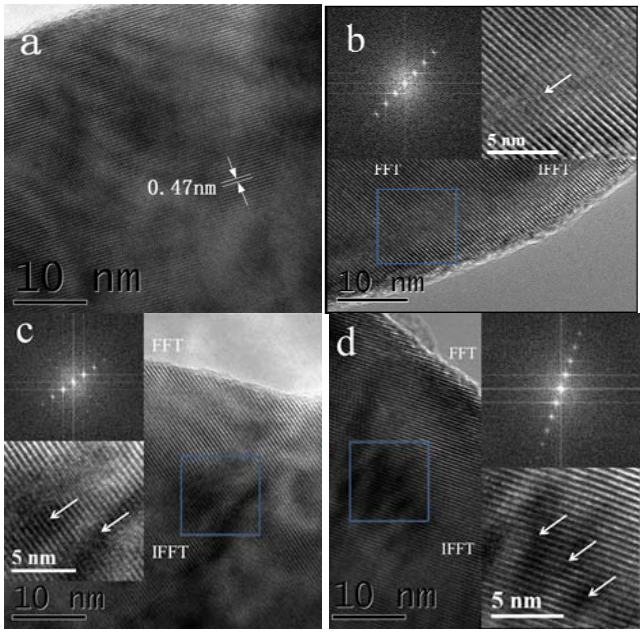

Fig. 3 TEM images of (a) LNMO, (b) LNMO-$Sn_{0.01}$, (c) LNMO-$Sn_{0.03}$, and (d) LNMO-$Sn_{0.05}$ samples. Fast Fourier Transform (FFT) and Inverse Fast Fourier Transform (IFFT) with selected area are presented.

To get a better understanding of the change of the covalent bonds after the Sn^{4+} substitution for Mn^{4+}, FTIR spectra of all the samples are shown in **Fig. 4**. For the LNMO sample, the characteristic peaks at 540 and 623 cm^{-1} are assigned to the asymmetric stretching modes of M-O bonds in MO_6 octahedra and the O-M-O bending modes.[36] For the Sn^{4+} substituted samples, the peaks at 540 cm^{-1} shift to lower wavenumber (533, 528, and 524 cm^{-1}), indicating the M-O covalency in Li-rich layered oxides is decreased after Sn^{4+} substitution. This is favorable for stabilization of the host lattice in Li-rich layered oxides. Some similar results have also been reported. For instance, Ti^{4+} or Ru^{4+} substitution for Mn^{4+} in the Li-rich layered $Li(Li_{0.20}Ni_{0.20}Mn_{0.6})O_2$ oxides can weaken the metal-oxygen covalence and lead to the lower oxygen loss from the lattice.[24,25] In addition, BO_4^{5-} doping $Li(Li_{0.2}Ni_{0.13}Co_{0.13}Mn_{0.54})O_2$ oxides

show a decreased M-O covalency bonds and O2p band top. The oxygen stability in those samples is enhanced and the host lattice of Li-rich layered oxides could be stabilized by adjusting the local electronic structure. [27] Therefore, it is an effective strategy by introducing Sn^{4+} into Li-rich layered oxides to the stabilize host lattice oxygen.

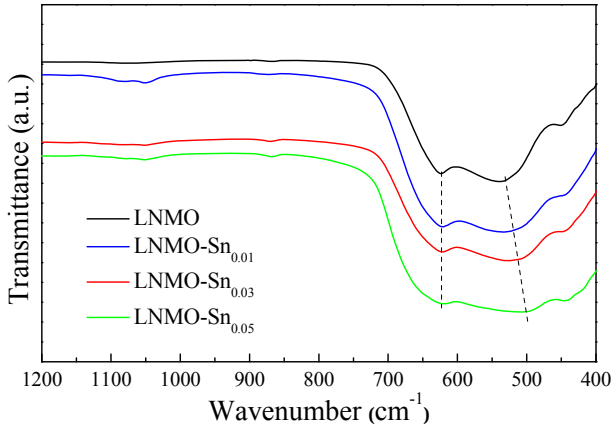

Fig. 4 FTIR spectra of the LNMO, LNMO-$Sn_{0.01}$, LNMO-$Sn_{0.03}$, and LNMO-$Sn_{0.05}$ samples.

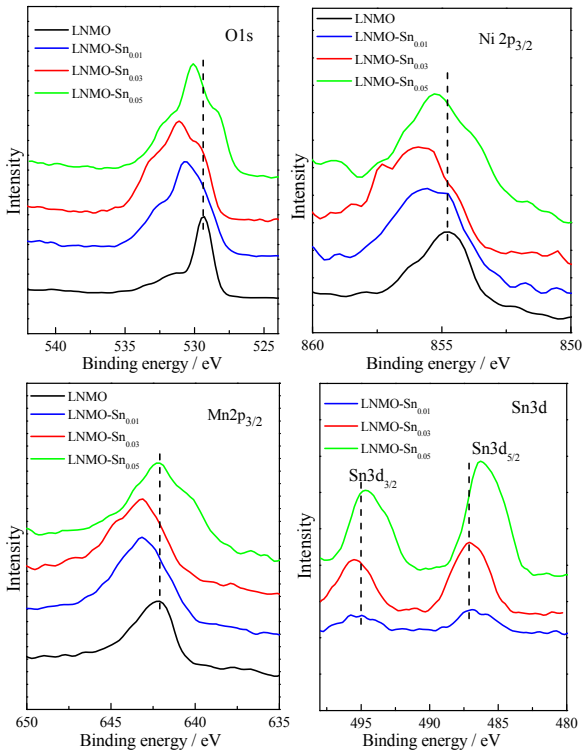

Fig. 5 XPS spectra of the LNMO, LNMO-$Sn_{0.01}$, LNMO-$Sn_{0.03}$, and LNMO-$Sn_{0.05}$ samples: O 1s, Mn 2p, Ni 2p, and Sn 3d core levels.

In order to identify the surface chemical states and bonding interaction between transition metals and oxygen before and after Sn^{4+} substitution, XPS is employed to characterize all the samples as shown in **Fig. 5**. The strong O1s peak at 529.4 eV for the LNMO sample, corresponds to the lattice oxygen of the Li-rich layered oxides,[16,37] and the standard NiO (529.6 eV).[38] It shifts to a higher binding energy (530.6, 531.2, and 530.1 eV) in the Sn^{4+} substituted samples due to a stronger electron interaction of oxygen and Sn^{4+} with a relatively high electronegativity (530.6 eV in the standard SnO_2).[38] The peaks located at 486.9, 487.1 and 486.3 eV in the LNMO-$Sn_{0.01}$, LNMO-$Sn_{0.03}$, and LNMO-$Sn_{0.05}$ samples are attributed to the existence of Sn^{4+} ($Sn3d_{5/2}$, 486.7 eV in the standard SnO_2), respectively.[38,39] The $Mn2p_{3/2}$ peak is located at 642.2 eV, close to the value of Mn^{4+}.[40] However, the $Mn2p_{3/2}$ peaks shift to a higher binding energy for the LNMO-$Sn_{0.01}$ and LNMO-$Sn_{0.03}$ samples due to the higher electronegativity of Sn^{4+}. Moreover, there is almost not any change for the LNMO-$Sn_{0.05}$ sample owing to the discrete SnO_2 particles. Compared with the LNMO sample, the binding energy of the $Ni2p_{3/2}$ in the Sn^{4+} subtituted samples becomes higher. The LNMO-$Sn_{0.01}$ and LNMO-$Sn_{0.03}$ samples exhibit wider peaks of $Ni2p_{3/2}$, which means a trace amount of the high oxidation state of Ni^{3+} on the surface. [41] It indicates that NiO is formed on the surface in all the samples due to the Ni preferential segregation,[42] which is well-known possible for Li-layered oxides. The fitted XPS peaks of LNMO-$Sn_{0.03}$ sample are shown in **Fig. S4**. The result suggests that the charge-state of Mn is only +4. The relative amount of Ni^{2+} is 92.98%, while relative amount of Ni^{3+} is only 7.02%. Specially, the LNMO-$Sn_{0.05}$ sample shows lower binding energy for all ions compared to the LNMO-$Sn_{0.03}$ sample, which should be due to that only partial Sn^{4+} substitutes Mn^{4+}, and other Sn^{4+} generates discrete SnO_2 phase in the LNMO-$Sn_{0.05}$ sample. Among all the samples, the LNMO-$Sn_{0.03}$ sample displays the highest binding energies of Ni , Mn, Sn, and O, indicating that there are the strongest M-O bonds and the most stable host lattice.

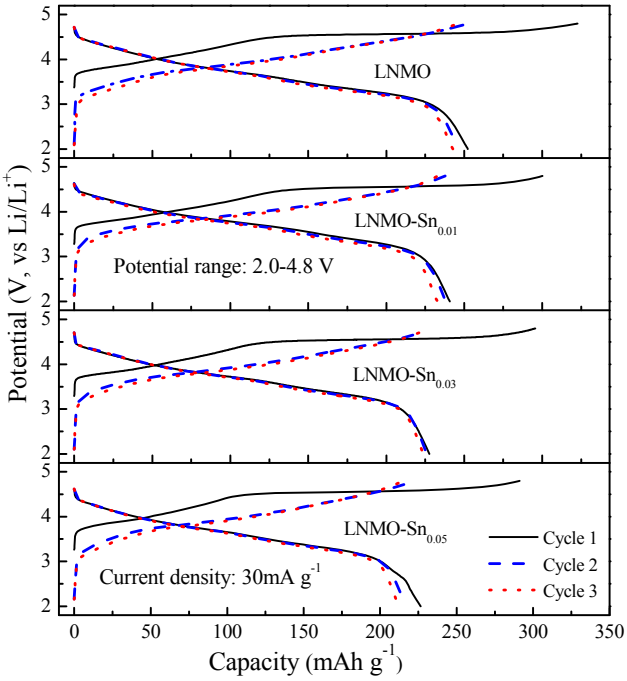

Fig. 6 The initial three charge–discharge curves of the LNMO, LNMO-$Sn_{0.01}$, LNMO-$Sn_{0.03}$, and LNMO-$Sn_{0.05}$ samples.

Fig. 6 shows the intial three charge–discharge curves of all the samples during cycling at the 0.1 C rate. For all the samples, there are two potential plateaus at 4.0 and 4.5 V in the initial charging, related to the nickel from Ni^{2+} to Ni^{4+} and the irreversible loss of oxygen as Li_2O from Li_2MnO_3.[10,43] Differently, the 4.5 V potential plateaus for the Sn^{4+} substituted samples are

shorter compared with the LNMO sample. It means that the oxidation of the O^{2-} ion to O_2 is suppressed by Sn^{4+} substitution in the Li-rich layered oxides during the initial charging. Therefore, the introduction of Sn^{4+} into Li-rich layered oxides is favorable for stabilization of the host lattice. In the following cycles, the potential plateaus of 4.5 V disappears, indicating that all the samples have structural rearrangement after the initial charging process.[44] The initial discharge capacities of the LNMO, LNMO-$Sn_{0.01}$, LNMO-$Sn_{0.03}$, and LNMO-$Sn_{0.05}$ samples are 257.3, 245.5, 232.2, and 226.5 mAh g^{-1}, respectively. The initial discharge capacity decreases with the Sn^{4+} amount increasing due to that the Sn^{4+} is electrochemically inert in the Li-rich layered oxides and can not easily be reduced to the low valence state of Sn^{2+} in the discharging process.[45] The initial three discharge curves of the LNMO-$Sn_{0.03}$ sample almost overlap, indicating the best reversibility among all of the samples. As known well, the voltage fade during the charge and discharge cycling is a great limit to the application of the Li-rich cathode materials. So the typical voltage profiles and differential capacity plots related to several cycles are presented (**Fig. S5**). During long cycling, the discharge capacity degradation of the LNMO sample is obvious, however, the LNMO-$Sn_{0.03}$ sample shows a slow degradation after 100 cycles. This indicates that the Sn^{4+} substitution for Mn^{4+} has the postive influence in the suppression of the local structure transition from the layered structure to layered/spinel coexistence.

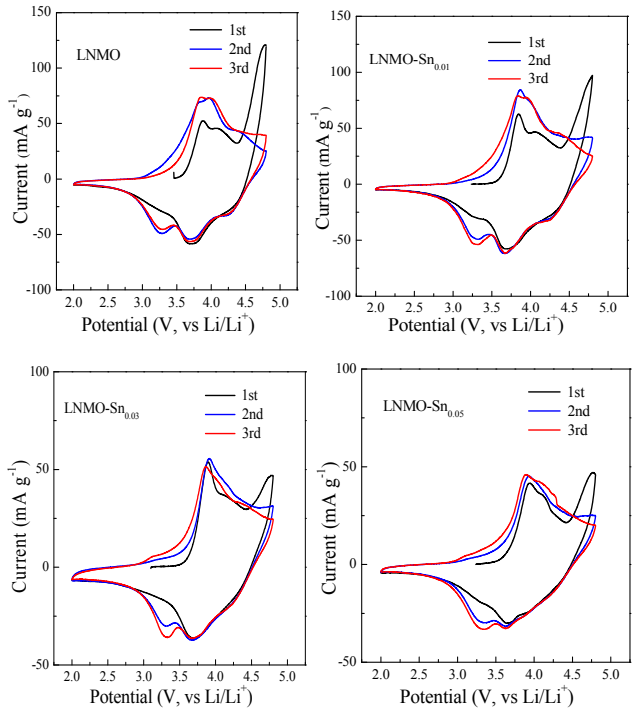

Fig. 7 Cyclic voltammograms of LNMO, LNMO-$Sn_{0.01}$, LNMO-$Sn_{0.03}$, and LNMO-$Sn_{0.05}$ samples at a scan rate of 0.1 mV s^{-1}.

Fig. 7 presents the CV curves of the LNMO and Sn^{4+} substituted samples at a scan of 0.1 mV s^{-1} from 2.0 to 4.8 V. For the LNMO sample, there are two oxidation peaks at 3.88 and 4.01 V in the initial anodic process, which can be attributed to the oxidation of the nickel from Ni^{2+} to Ni^{3+} and Ni^{3+} to Ni^{4+}, respectively. The peak located at 4.77 V is due to the loss of oxygen from the host lattice. The reduction peaks in the initial cathodic process at 4.26 and 3.71 V are assigned to the nickel from Ni^{4+} to Ni^{3+}, then to Ni^{2+}, respectively. The peak at 3.21V is related to the reduction reaction of manganese from Mn^{4+} to Mn^{3+}.[46,47] For the Sn^{4+} substituted samples, the peak current at 4.77 V in the initial anodic process decreases apparently as the Sn^{4+} amount increases, indicating that Sn^{4+} substitution for Mn^{4+} could suppress the oxygen loss during the initial oxidation process. Compared with the LNMO sample, in the initial three cycles, the oxidation and reduction peaks of the redox pair Ni^{3+}/Ni^{4+} are weaken for the Sn^{4+} substituted samples (x = 0.03 and 0.05). This phenomenon illustrates that the Sn^{4+} substituted samples have an accelerated electrochemical reaction. During the cathodic process in the initial three cycles, the LNMO-$Sn_{0.03}$ sample presents almost overlap reduction peak at the potential of 3.7 V, implying better electrochemical reversibility compared with other samples. The result is in agreement with the charge-discharge curves analysis.

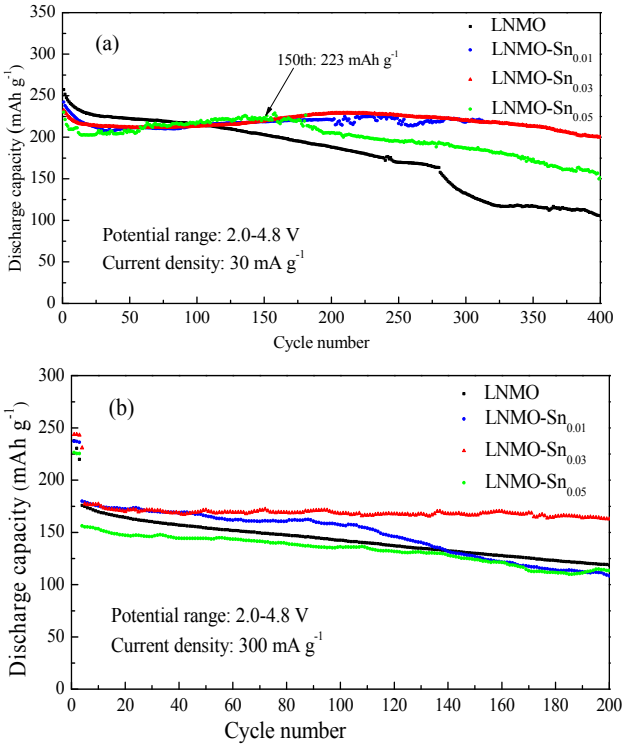

Fig. 8 Cycle performance of LNMO, LNMO-$Sn_{0.01}$, LNMO-$Sn_{0.03}$, and LNMO-$Sn_{0.05}$ samples at (a) 30 mA g^{-1} (b) 300 mA g^{-1}.

The cycle performance of the LNMO, LNMO-$Sn_{0.01}$, LNMO-$Sn_{0.03}$, and LNMO-$Sn_{0.05}$ samples is provided in **Fig. 8**. The coulombic efficiency of the LNMO, LNMO-$Sn_{0.01}$, LNMO-$Sn_{0.03}$, and LNMO-$Sn_{0.05}$ samples are 78.1, 80.2, 77.0 and 77.7%, respectively. At 0.1 C rate (30 mA g^{-1}), the LNMO-$Sn_{0.03}$ sample shows a superior cycling performance. It retains a high discharge capacity of 200 mAh g^{-1} after 400 cycles, showing a good discharge capacity retention of 86%. Relatively, the discharge capacity of the as-prepared LNMO sample is only 105.3 mAh g^{-1} after 400 cycles. The capacity retention is about 41%. The discharge capacities of Sn^{4+} substituted samples gradually increases with cycling and reaches 223 mAh g^{-1} in the 150th cycle at 0.1 C rate (Fig. 8a). It means that Sn^{4+} substitution for

Mn^{4+} could promote the activation of Li_2MnO_3 in Li-rich layered oxides during the long cycling. The enhanced cycle stability at the low rate could be ascribed to the stabilization of the host lattice by larger Sn^{4+} substitution for Mn^{4+} and the strengthen of the mental-oxygen bonds. After the initial 3 cycles for the activation at 0.1 C rate, the electrodes are charged and discharged at 1 C rate (300 mA g^{-1}) as shown in **Fig. 8b.** Apparently, the LNMO-$Sn_{0.03}$ sample delivers the optimized cycle performance among all the samples at high current density. The capacity retention is about 92% for the LNMO-$Sn_{0.03}$ sample after 200 cycles. At 5 C rate (1500 mA g^{-1}), the LNMO-$Sn_{0.03}$ sample has the highest initial discharge capacity and the superior cycle stability, showing good discharge capacity retention of 86% after 300 cycles (**Fig. S6**). The excellent high-rate performance and cycling stability are due to the lower cation mixing, larger lithum ion diffusion channel and more orderly layered structure after Sn^{4+} substitution.

The rate performance of the LNMO sample before and after Sn^{4+} substitution at various current density is presented in **Fig. 9**. All the samples do not show the excellent rate capability, and the effect of Sn^{4+} substitution on the rate performance is not obvious. At 5 C rate (1500 mA g^{-1}), the maximum discharge capacity of the LNMO-$Sn_{0.03}$ sample is 112.1 mAh g^{-1}, slightly larger than that of the LNMO sample (97.9 mAh g^{-1}). After cycling at 1500 mA g^{-1}, the capacity retention of the LNMO, LNMO-$Sn_{0.01}$, LNMO-$Sn_{0.03}$ and LNMO-$Sn_{0.05}$ samples are 40.2, 45.3, 48.5 and 43.5%, respectively. When the current density returns back to 30 mA g^{-1}, the good capacity retention of 94.7, 85.5, 96.0 and 86.1% is still obtained. Among all the samples, the LNMO-$Sn_{0.03}$ sample presents the highest capacity retention. It is noted that the LNMO-$Sn_{0.03}$ sample could better endure current density variation and has the prefer abuse performance than the LNMO sample.

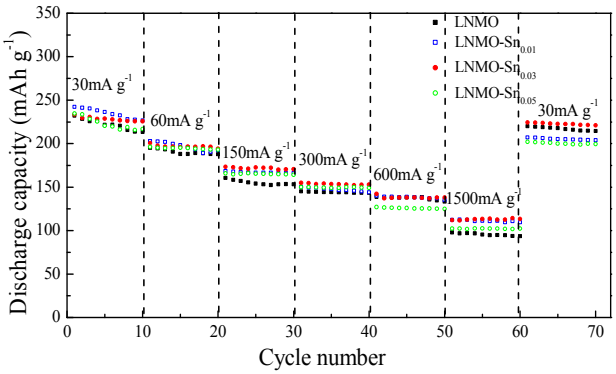

Fig. 9 Rate capabilities of LNMO, LNMO-$Sn_{0.01}$, LNMO-$Sn_{0.03}$, and LNMO-$Sn_{0.05}$ samples.

Electrochemical impedance spectra (EIS) are measured to get insight into the origin of the improvement in the electrochemical performance of Sn^{4+} substituted samples. **Fig. 10** presents Nyquist plots measured at fully discharged to 2.0 V at 0.1 C rate in different cycles. The plots of almost all the samples include two semicircles in the high-frequency and mid-frequency region, which correspond to the surface charge-transfer process and finite Nernst diffusion process. The sloped straight line in the low-frequency region is related to the Warburg diffusion process in the bulk. [48] The simulated electrochemical parameters are shown **Table S9** by using the equivalent circuit in **Fig. S7**, in which Rct means the surface charge-transfer resistance, Ws and Wo point to the finite Nernst diffusion impedance in the thin layer and semi-infinite Warburg diffusion impedance in the bulk, respectively. From the simulated electrochemical parameters, the surface charge-transfer resistance (471.9 Ω) is larger for the LNMO sample in the first cycle. It is decreased dramatically to 38.1 Ω in the second cycle and then increased slightly with cycling. It implies that there is an activation process in the initial electrochemical reaction. The surface charge-transfer resistance in the first cycle decreases with increase of Sn^{4+} content, suggesting the more rapid electrochemical reaction after Sn^{4+} substitution for Mn^{4+}. The results is in accordance with the CV analysis. Simultaneously, the Sn^{4+} substituted samples have a lower total diffusion impedance including finite Nernst diffusion and semi-infinite Warburg diffusion impedance. The above results indicate Sn^{4+} substitution for Mn^{4+} in Li-rich layered oxides could accelerate the surface charge-transfer and lithium ion diffusion processes. It is responsible for the improved cycling ability and high-rate capability. As measured by four-point probe method, the conductivity is 6.8 and 11*10^{-4} S·cm^{-1} for LNMO and LNMO-$Sn_{0.03}$ samples, indicating that the Sn-substitution can slightly improve the conductivity of LNMO sample.

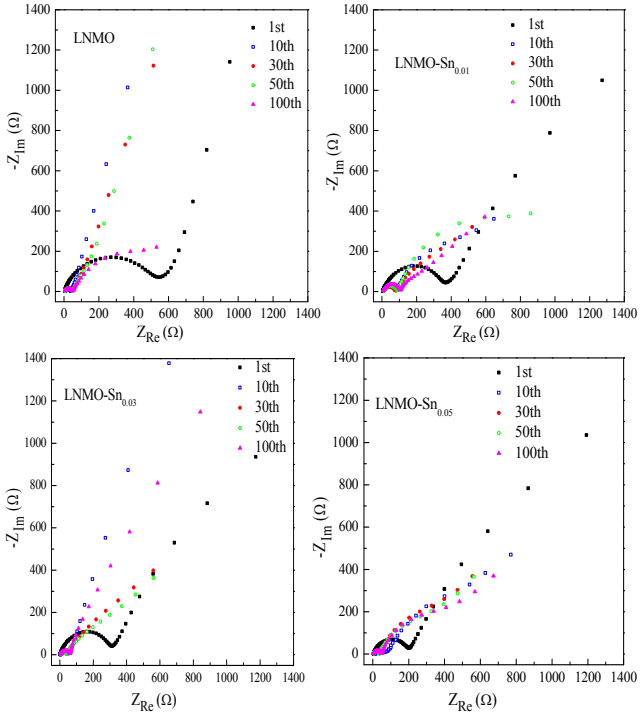

Fig. 10 Impedance spectra of LNMO, LNMO-$Sn_{0.01}$, LNMO-$Sn_{0.03}$, LNMO-$Sn_{0.05}$ samples.

The DSC profiles of LNMO and LNMO-$Sn_{0.03}$ electrodes after charging to 4.8 V (vs Li/Li^+) in the first cycle are displayed in **Fig. 11**. It is clear that the peak area of LNMO-$Sn_{0.03}$ sample (773.3 J/g) is lower than that of the sample (800.7 J/g). In addition, the onset temperature is higher for the LNMO-$Sn_{0.03}$ sample (218.9 °C) as compared with the as-prepared LNMO sample (211.6 °C). The above results indicate the heat amount originated from the charging process is reduced and thermal stability is definitely improved after the Sn^{4+} is introduced into Li-rich layered oxides to partially substitute Mn^{4+}. It is obvious

that the less oxygen loss lead to the weak side reaction between the active oxygen species and the electrolyte for the Sn^{4+} substituted samples.

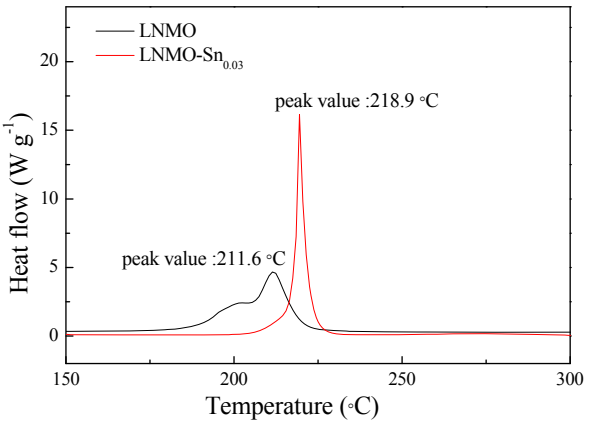

Fig. 11 DSC profiles of LNMO and LNMO-$Sn_{0.03}$ after charging to 4.8 V (vs Li/Li^+) in the first cycle.

Currently, many elements are used for improving performance of Li-rich layered oxides, such as Na^+, Mg^{2+}, Al^{3+}, Ti^{4+}, and Mo^{6+}, according to the different valence states and ionic radius. The effect of Sn^{4+} is similar to that of Ti^{4+} in decreasing of metal–oxygen covalence, reducing oxygen loss from the lattice and improving cycle stability of Li-rich layered oxides. However, it is different from the Na^+, Mg^{2+} and Al^{3+} ions, which are beneficial to improve the rate capability. The cation substitution by Sn^{4+} is proved to be effective for improving cycle stability of Li-rich layered oxides. Meanwhile, Sn^{4+} content in the oxides should be optimized. The degree of cation mixing is reduced and structure is more stable after introducing suitable Sn^{4+} content into Li-rich layered oxides. The significant improvement in electrochemical performance is attributed to the enlarged lithium ion diffusion channel, and strengthened bonding interaction between transition metals and oxygen. When the excessive Sn^{4+} substitute for Mn^{4+}, the crystallographic structure of the layered oxide is destroyed and undesired impurities appear, meanwhile, the bonding energy is decreased, resulting in the poor electrochemical performance.

Conclusions

The Li-rich layered $Li(Li_{0.17}Ni_{0.25}Mn_{0.58-x}Sn_x)O_2$ oxides are synthesized by a spray-drying method. It is noted that the suitable amount of Sn^{4+} substitution for Mn^{4+} is important in enhancing the electrochemical performance. It is indicated from XRD results that a more ordered layer structure is obtained due to the enlarged unit cell and lower cation mixing by the large Sn^{4+} substitution. The high electronegativity of Sn^{4+} with respect to Mn^{4+} is responsible for the strengthen bonding and weaken M-O covalency. Meanwhile, the oxidation of the O^{2-} ion to O_2 in the initial charging is suppressed by Sn^{4+} substitution, leading to the less structural transition. The introduction of Sn^{4+} into Li-rich layered oxides is favorable for stabilization of the host lattice. The sample with x=0.03 shows excellent cycle stability and high-rate capability as compared with the LNMO sample. Therefore, ion substitution by appropriate content of Sn^{4+} with large ionic radius and high electronegativity is an effective way to improve the structural stability and electrochemical performance of Li-rich layered oxides. The same strategy adopted in this work offer new insight and promising approach to explore and develop desired cathode materials for advanced lithum-ion batteries.

Acknowledgements

This work is supported by 973 Program (2015CB251100), NSFC (51272108 and 21421001), Research Fund for the Doctoral Program of Higher Education (20120031130002) and the TSFC (15JCYBJC21500) of China.

Notes and references

[a]*Institute of New Energy Material Chemistry, Collaborative Innovation Center of Chemical Science and Engineering (Tianjin), School of Materials Science and Engineering, Nankai University, Tianjin 300071, China. E-mail: xpgao@nankai.edu.cn; Fax: +86-22-2350-0876; Tel: +86-22-23500876*

[b]*Tianjin Key Laboratory of Metal and Molecule Based Material Chemistry, China*

† Electronic Supplementary Information (ESI) available: electrochemical performance of the sample, equivalent circuits, and simulated data from EIS of all the samples. See DOI: 10.1039/b000000x/

1 B. Dunn, H. Kamath and J. M. Tarascon, *Science*, 2011, **334**, 928.
2 X. P. Gao and H. X. Yang, *Energy Environ. Sci*., 2010, **3**, 174.
3 P. Y. Hou, L. Q. Zhang and X. P. Gao, *J. Mater. Chem. A*, 2014, **2**, 17130.
4 M. Bettge, Y. Li, B. Sankaran, N. D. Rago, T. Spila, R. T. Haasch, I. Petrov and D. P. Abraham, *J. Power Sources*, 2013, **233**, 346.
5 F. Dogan, B. R. Long, J. R. Croy, K. G. Gallagher, H. Iddir, J. T. Russell, M. Balasubramanian and B. Key, *J. Am. Chem. Soc*., 2015, **137**, 2328.
6 Y. K. Sun, M. J. Lee, C. S. Yoon, J. Hassoun, K. Amine and B. Scrosati, *Adv. Mater*., 2012, **24**, 1192.
7 G. L. Xu, Q. Wang, J. C. Fang, Y. F. Xu, J. T. Li, L. Huang and S. G. Sun, *J. Mater. Chem. A*, 2014, **2**, 19941.
8 H. J. Kim, H. G. Jung, B. Scrosati and Y. K. Sun, *J. Power Sources*, 2012, **203**, 115.
9 M. M. Thackeray, S. H. Kang, C. S. Johnson, J. T. Vaughey, R. Benedek and S. A. Hackney, *J. Mater. Chem*., 2007, **17**, 3112.
10 A. R. Armstrong, M. Holzapfel, P. Novak, C. S. Johnson, S. H. Kang, M. M. Thackeray and P. G. Bruce, *J. Am. Chem. Soc*., 2006, **128**, 8694.
11 C. R. Wu, X. P. Fang, X. W. Guo, Y. Mao, J. Ma, C. C. Zhao, Z. X. Wang and L. Q. Chen, *J. Power Sources*, 2013, **231**, 44.
12 Q. R. Xue, J. L. Li, G. F. Xu, H. W. Zhou, X. D. Wang and F. Y. Kang, *J. Mater. Chem. A*, 2014, **2**, 18613.
13 X. Feng, Z. Z. Yang, D. C. Tang, Q. Y. Kong, L. Gu, Z. X. Wang and L. Q. Chen, *Phys. Chem. Chem. Phys.*, 2015, **17**, 1257.
14 S. H. Guo, H. J. Yu, P. Liu, X. Z. Liu, D. Li, M. W. Chen, M. Ishida and H. S. Zhou, *J. Mater. Chem. A*, 2014, **2**, 4422.
15 W. Yuan, H. Z. Zhang, Q. Liu, G. R. Li and X. P. Gao, *Electrochim. Acta*, 2014, **135**, 199.
16 G. R. Li, X. Feng, Y. Ding, S. H. Ye and X. P. Gao, *Electrochim. Acta*, 2012, **78**, 308.
17 Q. Q. Qiao, H. Z. Zhang, G. R. Li, S. H. Ye, C. W. Wang and X. P. Gao, *J. Mater. Chem. A*, 2013, **1**, 5262.
18 Y. K. Sun, S. T. Myung, M. H. Kim, J. Prakash and K. Amine, *J. Am. Chem. Soc*., 2005, **127**, 13411.
19 X. K. Yang, D. Wang, R. Z. Yu, Y. S. Bai, H. B. Shu, L. Ge, H. P. Guo, Q. L. Wei, L. Liu and X. Y. Wang, *J. Mater. Chem. A*, 2014, **2**, 3899.
20 G. Z. Wei, X. Lu, F. S. Ke, L. Huang, J. T. Li, Z. X. Wang, Z. Y. Zhou and S. G. Sun, *Adv. Mater*., 2010, **22**, 4364.
21 W. He, D. D. Yuan, J. F. Qian, X. P. Ai, H. X. Yang and Y. L. Cao, *J. Mater. Chem. A*, 2013, **1**, 11397.
22 H. J. Xu, S. N. Deng and G. H. Chen, *J. Mater. Chem. A*, 2014, **2**, 15015.

23 N. Li, R. An, Y. F. Su, F. Wu, L. Y. Bao, L. Chen, Y. Zheng, H. F. Shou and S. Chen, *J. Mater. Chem. A*, 2013, **1**, 9760.

24 C. C. Wang and A. Manthiram, *J. Mater. Chem. A*, 2013, **1**, 10209.

25 J. C. Knight, P. Nandakumar, W. H. Kan and A. Manthiram, *J. Mater. Chem. A*, 2015, **3**, 2006.

26 H. Z. Zhang, Q. Q. Qiao, G. R. Li and X. P. Gao, *J. Mater. Chem. A*, 2014, **2**, 7454.

27 B. Li, H. J. Yan, J. Ma, P. R. Yu, D. G. Xia, W. F. Huang, W. S. Chu and Z. Y. Wu, *Adv. Funct. Mater.*, 2014, **24**, 5112.

28 H. Z. Zhang, Q. Q. Qiao, G. R. Li, S. H. Ye and X. P. Gao, *J. Mater. Chem*., 2012, **22**, 13104.

29 S. Hy, F. Felix, J. Rick, W. N. Su and B. J. Hwang, *J. Am. Chem. Soc.*, 2014, **136**, 999.

30 L. Chen, Y. F. Su, S. Chen, N. Li, L. Y. Bao, W. K. Li, Z. Wang, M. Wang and F. Wu, *Adv. Mater*., 2014, **26**, 6756.

31 W. He, J. F. Qian, Y. L. Cao, X. P. Ai and H. X. Yang, *RSC Adv*., 2012, **2**, 3423.

32 S. H. Guo, S. C. Zhang, X. M. He, W. H. Pu, C. Y. Jiang and C. R. Wan, *J. Electrochem. Soc.*, 2008, **155**, A760.

33 S. X. Liao, Y. J. Zhong, B. H. Zhong, H. Liu and X. D. Guo, *J. Power Sources*, 2014, **246**, 569.

34 P. K. Nayak, J. Grinblat, M. Levi and D. Aurbach, *Electrochim. Acta*, 2014, **137**, 546.

35 X. W. Wang, X. P. Gao, G. R. Li, T. Y. Yan and H. Y. Zhu, *J. Phys. Chem. C*, 2008, **112**, 5384.

36 M. Y. Hou, J. L. Liu, S. S. Guo, J. Yang, C. X. Wang and Y. Y. Xia, *Electrochem. Commun*., 2014, **49**, 83.

37 J. Mun, J. H. Park, W. Choi, A. Benayad, J. H. Park, J. M. Lee, S. G. Doo and S. M. Oh, *J. Mater. Chem. A*, 2014, **2**, 19670.

38 C. D. Wagner, W. M. Riggs, L. E. Davis and J. F. Moulder, *Handbook of X-ray Photoelectron Spectroscopy*, Perkin-Elmer Corporation, Physical Electronics Division, USA, 1st edn,1979.

39 C. Hou, X. M. Shi, C. X. Zhao, X. Y. Lang, L. L. Zhao, Z. Wen, Y. F. Zhu, M. Zhao, J. C. Li and Q. Jiang, *J. Mater. Chem. A*, 2014, **2**, 15519.

40 W. Choi, A. Benayard, J. H. Park, J. Park, S. G. Doo and J. Mun, *Electrochim. Acta*, 2014, **117**, 492.

41 C. R. Fell, K. J. Carroll, M. F. Chi and Y. S. Meng, *J. Electrochem. Soc*., 2010, **157**, A1202

42 M. Gu, I. Belharouak, A. Genc, Z. G. Wang, D. P. Wang, K. Amine, F. Gao, G. W. Zhou, S. Thevuthasan, and D. R. Baer, *Nano Lett*., 2012, **12**, 5186.

43 R. Z. Yu, X. Y. Wang, D. Wang, L. Ge, H. B. Shu and X. K. Yang, *J. Mater. Chem. A*, 2015, **3**, 3120.

44 C. R. Fell, D. H. Lee, Y. S. Meng, J. M. G. Amores, E. Moran and M. E. A. Dompablo, *Energy Environ. Sci.*, 2012, **5**, 6214.

45 M. Sathiya, G. Rousse, K. Ramesha, C. P. Laisa , H. Vezin, M. T. Sougrati, M. L. Doublet, D. Foix, D. Gonbeau, W. Walker, A. S. Prakash, M. B. Hassine, L. Dupont and J. M. Tarascon, *Nat. Mater.*, 2013, **12**, 827.

46 Q. Fu, F. Du, X. F. Bian, Y. H. Wang, X. Yan, Y. Q. Zhang, K. Zhu, G. Chen, C. Z. Wang and Y. J. Wei, *J. Mater. Chem. A*, 2014, **2**, 7555.

47 W. W. Zhao, S. Yamamoto, A. Tanaka and H. Noguchi, *Electrochim. Acta*, 2014, **143**, 347.

48 F. Kuang, D. Zhang, Y. J. Li, Y. Wan and B. R. Hou, *J. Solid State Electrochem.*, 2009, **13**, 385.